Article:
Liu, Y, Zhao, M, He, T et al. (2 more authors) (2023) Formation of molar tooth structures in low sulfate Precambrian oceans. Geochimica et Cosmochimica Acta, 354. pp. 62-73. ISSN 0016-7037

https://doi.org/10.1016/j.gca.2023.06.013

Formation of molar tooth structures in low sulfate Precambrian oceans

Yang Liu[a, b*], Mingyu Zhao[c], Tianchen He[d], Xingqi Li[b], Simon W. Poulton[e]

[a] *College of Environmental Science and Engineering, Dalian Maritime University, Dalian 116026, China.*

[b] *School of Energy resource, China University of Geosciences (Beijing), Beijing 100083, China.*

[c] *Key Laboratory of Cenozoic Geology and Environment, Institute of Geology and Geophysics, Chinese Academy of Sciences, Beijing 100029, China.*

[d] *College of Oceanography, Hohai University, Nanjing 210024, China.*

[e] *School of Earth and Environment, University of Leeds, Leeds LS2 9JT, UK.*

Corresponding Author: yangliu@cugb.edu.cn

Abstract

Molar tooth structures (MTS) comprise calcite microspar-filled voids in fine-grained shallow-water carbonate, and were commonly formed in the Mesoproterozoic and early Neoproterozoic. However, the origin of MTS and links between the temporal distribution of MTS and contemporaneous seawater chemistry remains poorly understood. Here we report elemental and isotopic data for MTS and host rocks from the Mesoproterozoic Gaoyuzhuang Formation (~1,600–1,550 Ma), North China Craton. The results reveal similar C, S and Sr isotope signatures between MTS and host rocks, which are close to the isotopic compositions of contemporaneous global seawater, suggesting an early diagenetic, seawater-buffered origin for MTS. A small sulfur isotopic fractionation between seawater sulfate and pyrite ($\Delta^{34}S_{CAS\text{-}Py}$) of 4.1 ± 1.5‰ in host rocks is consistent with previously reported data, providing support for sub-millimolar sulfate concentrations in Mesoproterozoic seawater. Our observations suggest that the widespread occurrence of MTS through the Mesoproterozoic to early Neoproterozoic was broadly linked to sulfate scarcity in the ocean. We further propose that in Proterozoic oceans with sub-millimolar seawater sulfate concentrations, where aerobic and anaerobic methane oxidation was likely inhibited, methane produced via methanogenesis may have been more prone to accumulate in sediments, creating voids during escape. The absence of MTS across periods of higher sulfate concentrations during the Palaeoproterozoic and after the mid-Neoproterozoic, suggests that elevated sulfate concentrations promoted consumption of methane via anaerobic methane oxidation, thus preventing methane accumulation and the formation of sediment voids. Rapid lithification of the substrate as a result of elevated

carbonate saturation may have also hindered the formation of MTS during these intervals. The link between MTS and changes in both oceanic sulfate levels and benthic methane fluxes gives a new perspective on temporal fluctuations in Earth's redox state through time.

Key words: Molar tooth structures; Seawater-buffered diagenesis; Seawater sulfate; Mesoproterozoic; Precambrian.

1. Introduction

Molar tooth structures (MTS) are commonly preserved in Precambrian shallow-water carbonate successions (Shields, 2002; Pollock et al., 2006; Kriscautzky et al., 2022). They occur predominantly within fine-grained, clay rich carbonate rocks, and are more rarely recorded in coarse-grained carbonate and siliciclastic rocks (Pollock et al., 2006; Hodgskiss et al., 2018). MTS exhibit a variety of morphologies, but typically occur as linear, sheet-like ribbons and spheroids (blobs or bubbles). Ribbon MTS can range from a few millimeters to several centimeters in width and a few to tens of centimeters in length, whereas bubble MTS can range from a few millimeters to several centimeters in diameter (Pollock et al., 2006; Kriscautzky et al., 2022). In many cases, MTS with different morphologies intersect in three dimensions to form complex interconnection networks (Furniss et al., 1998; Pratt, 1998; Pollock et al., 2006; Kriscautzky et al., 2022). MTS are filled with uniform, equant calcite microspar crystals ranging from 5 to 15 μm in diameter (Frank and Lyons, 1998; Furniss et al., 1998; Pollock et al., 2006).

Morphological, sedimentological and geochemical evidence suggests that MTS

comprise early diagenetic structures that were formed proximal to the sediment-water interface (SWI) before sediment compaction and lithification (Pollock et al., 2006; Hodgskiss et al., 2018; Kuang, 2014; Kriscautzky et al., 2022). The origin of MTS has long been debated and various hypotheses have been proposed. The formation of MTS requires the initial generation of voids within unlithified sediments. Proposed mechanisms of void formation include gas expansion and migration (Furniss et al., 1998; Shen et al., 2016), seismic activity (Pratt, 1998), wave-pumping (Bishop and Sumner, 2006), and a combination of wave loading and shrinking of clay minerals (Hodgskiss et al., 2018). In addition, a variety of biogeochemical processes are prerequisites for the rapid precipitation of carbonate microspar into voids before sediment compaction, including iron reduction (Hodgskiss et al., 2018) and microbial sulfate reduction (Frank and Lyons, 1998; Shen et al., 2016).

Molar tooth structures occur in late Archean and Proterozoic rocks, but are most abundant and widespread through parts of the Mesoproterozoic to early Neoproterozoic, becoming extremely rare after ~750 Ma (James et al., 1998; Shields, 2002; Hodgskiss et al., 2018; Kriscautzky et al., 2022). The disappearance of MTS from the geological record has variously been linked to seafloor substrate renovation and bioturbation by metazoans (Frank and Lyons, 1998; Pratt, 1998), a decline in seawater carbonate saturation (Pollock et al., 2006; Kah and Bartley, 2022; Kriscautzky et al., 2022), an increase in carbonate precipitation inhibitors (Shields, 2002), deep ocean ventilation and oxygenation (Shen et al., 2016), and a decrease in smectite abundance in marine sediments (Hodgskiss et al., 2018). The temporal record of MTS suggests that its occurrence may have been linked to

shifts in the biogeochemistry of marine environments (Shields, 2002; Pollock et al., 2006; Hodgskiss et al., 2018). Hence, MTS have great potential to provide insight into the evolution of marine environments during the Precambrian. However, both the origin of MTS, and potential links between MTS formation and the evolution of Earth's surface environment, remain poorly understood.

Here we present carbon and oxygen, carbonate-associated sulfate (CAS), pyrite sulfur and strontium isotope data, combined with diagenetically-diagnostic elemental data, for MTS and associated matrix carbonate from the Mesoproterozoic Gaoyuzhuang Formation (~1,600–1,550 Ma) of the North China Craton. Our approach allows a detailed assessment of the marine chemical conditions driving the formation of MTS, and provides insight into potential links between MTS formation and the evolution of marine chemistry through Earth's history.

2. Geological setting

The Yanliao aulacogen developed on the eastern margin of the North China Craton (Fig. 1), which was connected to the open ocean during the Proterozoic (Qiao and Gao, 2007). In the study area, an ~9-km-thick succession of Proterozoic strata was deposited on Archean-Paleoproterozoic crystalline basement. In ascending order, the strata comprise the Paleoproterozoic Changcheng Group (~1,650–1,600 Ma), the Mesoproterozoic Jixian Group (~1,600–1,400 Ma), an unnamed group (~1,400–1,000 Ma), and the unconformably overlying Neoproterozoic Qingbaikou Group (~1,000–800 Ma) (Fig. 1; Lu et al., 2008).

The Gaoyuzhuang Formation (~1,600–1,550 Ma) is the lowermost formation of the Jixian

Group, and consists mainly of shallow marine carbonate rocks (dolostone and limestone) deposited in a supratidal to distal shelf setting (Guo et al., 2015). The Gaoyuzhuang Formation can be subdivided into four lithological members in the Jizhou area (Luo et al., 2021; Zhang et al., 2018). In ascending order, Member I (the Guandi Member) consists mainly of cherty dolomicrite, microbial dolomicrite and stromatolitic dolomicrite, with ripple-marked sandstone at the base. Member II (the Sangshu'an Member) is composed mainly of thin bedded, Mn-rich dolomicrite underlying moderate to thick dolostone. The lower part of Member III (the Zhangjiayu Member) consists mainly of limestone and dolomitic limestone, with limestone, bedded muddy dolostone, laminated carbonate and interbedded black shale. The upper part of Member III is dominated by microbial carbonates, including dolomitic limestone and micritic limestone with molar tooth structures. Member IV mainly comprises bituminous lamellar dolostone, coarse-grained stromatolitic dolostone, dolomicrite, and overlying dolostone with cherty concretions (Luo et al., 2021; Zhang et al., 2018).

In the Gaoyuzhuang Formation, MTS are concentrated in micritic limestone of the upper part of Member III. In outcrop, MTS are visible on weathered rock surfaces and occur as distinct lithologies with sharp boundaries within micritic carbonate host rocks. The morphology of the MTS can be divided into several types, including banded, ribbons and spheroids of varying size (Fig. 2). In plan view, ribbon MTS are typically a few millimeters to centimeters in width and several to tens of centimeters in length. In vertical profile, they display ptygmatically folded morphologies and are commonly oriented vertically or obliquely with respect to bedding. Ribbon MTS occasionally appear as small protrusions

from banded and spheroidal MTS. Spheroidal MTS (bubbles or blobs) are typically a few millimeters to centimeters in diameter and are often connected. The co-occurrence of multiple MTS morphologies within the same substrate suggests a common origin. In thin section, MTS have sharp contacts with the surrounding matrix and typically lack detrital infill, suggesting that molar tooth microspar was precipitated in situ predominantly beneath the SWI within the shallow substrate (Pollock et al., 2006; Kriscautzky et al., 2022). Molar tooth microspar is composed of uniform, equant, polygonal, tightly packed, ~10–15 μm microcrystalline calcite. The host rock has a dominantly fine-grained micritic matrix with sporadic small, non-interlocked, euhedral or subhedral dolomite crystals (Fig. 2).

A zircon U-Pb (LA-MC-ICPMS) age of 1,577 ± 12 Ma (Tian et al., 2015) was reported from a tuff bed in the lower part of Member III in the Jizhou area. A tuff bed in the upper part of Member III of the Gaoyuzhuang Formation in the Yanqing County, northwestern Beijing, yielded a zircon U-Pb (LA-MC-ICPMS) age of 1,560 ± 5 Ma (Li et al., 2010). The Gaoyuzhuang strata has experienced only low-grade (below prehnite-pumpellyite facies) metamorphism (Chu et al., 2007).

3. Materials and Methods

3.1 Sample preparation

Molar tooth structures and associated host carbonate samples were collected from Member III of the Gaoyuzhuang Formation in Jizhou District (40.1451°N, 117.4544°E), ~100 km east of Beijing, China (Fig. 1). Prior to geochemical analyses, bulk rock samples were trimmed to avoid veins and weathered surfaces. We did not observe visible pyrite

nodules or bands in our samples, although our sampling strategy does not preclude the possible inclusion of disseminated pyrite. Approximately 100 g of host carbonate rock sample was crushed using an agate mortar. Sample powders from ribbon MTS were carefully drilled to a shallow depth to avoid potential contamination from host rock. In view of the thin and sinuous nature of ribbon MTS, in most cases it was impossible to collect enough sample powder from a single ribbon sample. Therefore, powders were drilled from several ribbon MTS from the same hand-sample and homogenized. Ribbon MTS were not selected for CAS extraction, because the traditional extraction method used here generally requires >20 g of powder and it was not possible to collect sufficient sample powder without contamination from the host rock. Bubble and banded MTS samples were carefully split using a rock saw to separate from the host rock, and then polished to further avoid potential contamination from the host rock. These polished MTS samples (~50 g each) were then powdered using an agate mill. All geochemical analyses were conducted at the State Key Laboratory of Biogeology and Environmental Geology (BGEG), China University of Geosciences, Wuhan.

3.2 Elemental analyses

Approximately 50 mg of sample powder from MTS and host rock was leached sequentially twice in 0.3% acetic acid (Li et al., 2011). The leached solutions were collected for elemental analyses and strontium isotope analyses. Major elements were analyzed using a Thermo Fisher iCAP 7400 inductively coupled plasma optical emission spectrometry (ICP-OES), and trace elements were analyzed using an Agilent 7700x inductively coupled plasma mass spectrometer (ICP-MS). Analytical precision was better

than 5% (1σ) for all reported data, based on replicate analyses of two USGS standards (AGV-2, andesite; BCR-2, basalt) and two Chinese national standards (GSR-1, granite; GSR-6, carbonate).

3.3 Pyrite and CAS extractions, and sulfur isotope analyses

Pyrite sulfur was extracted following the chromium reduction method (Canfield et al., 1986), which is briefly described here. About 5 g of sample powder from MTS and host rock was heated under N_2 for 2 h after addition of 20 ml of 12 M HCl and 40 ml of 1 M $CrCl_2$ solution. The liberated hydrogen sulfide was trapped in ~30 ml of silver nitrate in order to precipitate silver sulfide (Ag_2S). For CAS extractions, ~20–50 g of sample powder from MTS (bubble and banded) and host rock was treated in 10% NaCl solution for 24 h and then washed three times with deionized water to remove non-CAS sulphate. This step was repeated several times (He et al., 2019) until there was no barite ($BaSO_4$) precipitation from the supernatant upon addition of saturated $BaCl_2$ solution (~250 g/L). The cleaned powder was then treated with 4 M HCl to dissolve carbonate, until the reaction was complete. The filtered solution was treated with 125 ml of saturated $BaCl_2$ to precipitate sulphate as $BaSO_4$. The CAS concentrations were measured using ICP-OES and gravimetric methods, and the results showed good agreement between the two methods.

The Ag_2S and $BaSO_4$ precipitates from pyrite and CAS extractions were filtered, dried and homogenized, and were then combusted with an excess of V_2O_5 to measure the sulfur isotopic compositions of pyrite ($\delta^{34}S_{Py}$) and CAS ($\delta^{34}S_{CAS}$) on a Thermo Fisher Scientific Delta V Plus isotope ratio mass spectrometer (IRMS) coupled with a Flash elemental analyzer. The $\delta^{34}S_{Py}$ data were calibrated using three IAEA standards: IAEA-S1 (–0.3‰),

IAEA-S2 (+22.7‰) and IAEA-S3 (–32.5‰), and $\delta^{34}S_{CAS}$ data were calibrated using three additional IAEA standards: NBS-127 (+20.3‰), IAEA-SO-5 (+0.5‰) and IAEA-SO-6 (–34.1‰). Sulfur isotope compositions are reported in δ-notation as permil (‰) relative to the Vienna Canyon Diablo troilite (V-CDT). Analytical precision was better than ±0.3‰ (1σ) based on replicate analyses of IAEA standards.

3.4 Carbon and oxygen isotope analyses

For carbonate $\delta^{13}C$ and $\delta^{18}O$ analyses, about 50–300 μg of dried sample powder from MTS and host rock was reacted with 100% phosphoric acid at 70°C. The resulting CO_2 was subsequently introduced into a MAT 253 isotope ratio mass spectrometer (IRMS) for isotopic measurements. The $\delta^{13}C$ and $\delta^{18}O$ data were calibrated relative to international reference standard NBS-19 ($\delta^{13}C$ = +1.95‰; $\delta^{18}O$ = −2.20‰) and Chinese national standard GBW04416 ($\delta^{13}C$ = +1.61‰; $\delta^{18}O$ = −11.59‰). Results are reported in permil notation relative to Vienna Pee Dee Belemnite (VPDB), with a precision of better than ±0.1‰ (1σ).

3.5 Strontium isotope analyses

Generally, samples with relatively high Sr concentrations (>600 ppm) and low Mn/Sr ratios (<0.2) were selected for Sr isotope measurements. However, three samples with lower Sr concentrations (200–400 ppm) and higher Mn/Sr ratios (0.2–0.4) were also analyzed for comparison. The leached solutions were dried at 120°C and dissolved in 1 ml of 3 M double-distilled nitric acid, followed by Sr purification using standard Sr-spec resin ion-chromatography. Sr isotope compositions were measured on a Nu Plasma II multi-collector inductively coupled plasma mass spectrometer (MC-ICP-MS). Mass fractionation

was normalized to an assumed $^{86}Sr/^{88}Sr$ ratio of 0.1194 (Nier, 1938). The NIST SRM 987 standard was analyzed along with the samples and yielded an average $^{87}Sr/^{86}Sr$ ratio of 0.71022 ± 0.00001 (2sd, n = 8). Data reported here have been normalized to the recommended NIST SRM 987 standard value of 0.710248 (McArthur et al., 2012).

4. Results

MTS and host carbonate rock samples from Member III of the Gaoyuzhuang Formation generally have low Mn (<150 ppm) and elevated Sr (>300 ppm) concentrations. Mn concentrations range from 17.1 to 118.4 ppm (mean = 71.1 ± 32.4 ppm) for MTS, and from 35.5 to 124.6 ppm (mean = 85.7 ± 30.6 ppm) for host rocks. Sr concentrations range from 434.5 to 836.8 ppm (mean = 693.7 ± 95.4 ppm) for MTS, and from 272.1 to 983.2 ppm (mean = 544.5 ± 269.8 ppm) for host rocks. Both the MTS and host rocks generally have low Mn/Sr (ppm/ppm) and Mg/Ca (wt%/wt%) ratios, but MTS exhibit lower values (Mn/Sr = 0.10 ± 0.04, Mg/Ca = 0.08 ± 0.02) relative to the host rocks (Mn/Sr = 0.18 ± 0.09, Mg/Ca = 0.25 ± 0.08).

Carbonate $\delta^{13}C$ values of MTS and host rocks vary within a narrow range (−1.0 to +0.4‰), with an average of −0.3 ± 0.4‰ (1σ) for MTS and −0.1 ± 0.3‰ (1σ) for host rocks. The $\delta^{18}O$ values for the MTS and host rocks vary between −6.8‰ and −4.2‰, with averages of −6.0 ± 0.3‰ (1σ) and −5.3 ± 0.7‰ (1σ), respectively. Pyrite concentrations are generally low in both MTS and host rocks, ranging from values below detection to 135 ppm for MTS (mean = 88 ± 23 ppm), and from values below detection to 142 ppm (mean = 81 ± 31 ppm) for host rocks. CAS concentrations range from below detection to 109 ppm

(mean = 57 ± 34 ppm) for MTS, and from values below detection to 243 ppm (mean = 94 ± 68 ppm) for host rocks. Pyrite sulfur isotopes ($\delta^{34}S_{Py}$) have a relatively narrow distribution (8.0−12.4‰), with an average of 10.6 ± 1.5‰ (1σ) for MTS and 9.5 ± 1.1‰ (1σ) for host rocks. CAS sulfur isotopes ($\delta^{34}S_{CAS}$) range from 9.1 to 16.1‰, with an average of 13.7 ± 2.7‰ (1σ) for MTS and 12.4 ± 0.7‰ (1σ) for host rocks. Strontium isotope ratios ($^{87}Sr/^{86}Sr$) range from 0.70524 to 0.70681 for MTS, and from 0.70539 to 0.70753 for host rocks (Supplementary Table S1).

5. Discussion

5.1 Evaluation of diagenetic alteration and dolomitization

We evaluate the degree of diagenetic alteration and dolomitization using petrographic analyses, and element and oxygen isotope systematics. Petrographic analyses can provide a first-order assessment of diagenesis. In our samples from Member III of the Gaoyuzhuang Formation, the host rock mainly consists of micritic matrix with sporadic small, non-interlocked, euhedral or subhedral dolomites that show little evidence for increased crystal sizes associated with recrystallization, suggesting very early dolomitization. The MTS are composed of uniform, equant calcite microspar and generally lack more coarsely crystalline phases (Fig. 2). The finely crystalline nature of MTS and host rock suggests limited diagenetic alteration.

The oxygen isotope composition of carbonate rocks is generally considered a sensitive indicator for diagenetic evaluation (Banner and Hanson, 1990). The $\delta^{18}O$ values of most MTS and host rock samples range from −5 to −7‰, which are similar to those recorded by

most well-preserved, non-evaporitic Mesoproterozoic carbonate rocks (e.g., Kah et al., 2012; Gilleaudeau and Kah, 2013; Guo et al., 2015). Furthermore, all samples show consistently low Mg/Ca ratios, and a lack of correlation between $\delta^{18}O$ and both $\delta^{13}C$ and Mg/Ca (Fig. 3) suggests that MTS and host rocks formed with only limited diagenetic alteration or dolomitization. Strontium is typically rapidly lost during post-depositional diagenesis (Brand and Veizer, 1980, Banner and Hanson, 1990). Generally elevated Sr concentrations in the MTS (434.5 to 836.8 ppm) and host rock (272.1 to 983.2 ppm), combined with oxygen isotope compositions within the range of well-preserved marine carbonate rocks, suggest a primary aragonitic phase. The consistently lower Mn/Sr and Mg/Ca ratios of MTS compared to those of the host rocks (Fig. 3) could be due to minor dolomitization in the host rock phase, consistent with petrographic observations. These systematic differences are consistent with those previously reported for MTS strata worldwide (Table 1, Shen et al., 2016; Hodgskiss et al., 2018), suggesting that MTS were more resistant to post-depositional alteration than the penecontemporaneous host rocks. This is further supported by lower $^{87}Sr/^{86}Sr$ values in MTS relative to those of the host rocks (Fig. 5), because diagenetic alteration of carbonate generally results in elevated $^{87}Sr/^{86}Sr$ ratios (e.g., Kaufman et al., 1993).

Carbonate-associated sulfate (CAS) represents marine sulfate preserved in the sedimentary carbonate lattice, and its sulfur isotope composition ($\delta^{34}S_{CAS}$) in well-preserved carbonate rocks is commonly considered to represent the contemporaneous seawater sulfate-sulfur isotopic composition (e.g., Kah et al., 2004; Gill et al., 2008). Indeed, a direct comparison of the sulfur isotope composition of CAS and coeval barite in marine

sediments deposited over the last 25 Myr showed a close consistency of ± 2‰ (Rennie and Turchyn, 2014). However, the isotopic composition and abundance of CAS may be altered by diagenetic processes (Gill et al., 2008; Rennie and Turchyn, 2014) or experimental contamination during CAS extraction (Wotte et al., 2012). In addition, complex carbonate components may potentially result in variability in bulk-rock $\delta^{34}S_{CAS}$ values across small spatial scales (Fike et al., 2015). Nevertheless, in our MTS and host rock samples, no statistically significant correlation was observed between $\delta^{34}S_{CAS}$ and traditional indicators of diagenesis (e.g., Mn/Sr, Mg/Ca and CAS concentration; Fig. 4), indicating that the $\delta^{34}S_{CAS}$ values are unlikely to have been significantly affected by diagenetic alteration. In addition, it has also been suggested that while CAS concentrations generally decrease during diagenesis, $\delta^{34}S_{CAS}$ values are highly resistant to diagenetic processes (Lyons et al., 2005; Fichtner et al., 2017). Previous studies have shown that pyrite oxidation may occur during the CAS extraction procedure (Marenco et al., 2008; Mazumdar et al., 2008), thereby potentially affecting CAS sulfur isotope compositions. In this study, we applied consecutive NaCl washes before the CAS extraction to minimize the potential for contamination from pyrite oxidation and other non-CAS phases during the CAS extraction. If pyrite oxidation affected the $\delta^{34}S_{CAS}$ values significantly, contamination by pyrite-derived sulfate would be expected to lower the $\delta^{34}S_{CAS}$ values. However, the $\delta^{34}S_{CAS}$ values of MTS (13.7 ± 2.7‰) and host rock (12.4 ± 0.7‰) are consistent with both published $\delta^{34}S_{CAS}$ values from Member III of the Gaoyuzhuang Formation (Luo et al., 2015; Guo et al., 2015; Ma et al., 2023), and a global $\delta^{34}S_{CAS}$ compilation from ~1.5−1.6 Ga (Luo et al., 2015, and references therein), suggesting that the $\delta^{34}S_{CAS}$ values obtained in this

study approximate primary isotopic compositions.

5.2 Potential origins of MTS formation

Various models for the formation of cracks and voids in MTS have been proposed. The seismic model suggests that microspar originated within the host rock as a fine-grained detrital component and was segregated from the sediment matrix during liquefaction of the substrate as a result of seismic shaking (Pratt, 1998). However, petrographic evidence indicates that MTS in the Gaoyuzhuang Formation commonly have a sharp contact with the host rocks, and microspar is typically distinguishable from the sediment matrix (Fig. 2), consistent with global-scale observations of molar tooth microspar occurring primarily within cracks and voids (Kriscautzky et al., 2022). Although recent cathodoluminescence (CL) petrographic evidence has revealed that molar tooth microspar may also occur in the form of individual crystals to small patches within the sediment matrix (Kriscautzky et al., 2022), the two-phase (core and rim) nature of the microspar suggests that it is likely to be precipitated in situ in pore spaces as a cement phase, rather than being a detrital component (Pollock et al., 2006; Kriscautzky et al., 2022). Wave loading (Bishop and Sumner, 2006), or reduction of iron in smectite (and associated conversion of smectite to illite) coupled with wave loading, have also been proposed to explain the initial formation of voids in MTS (Hodgskiss et al., 2018). However, MTS in the Gaoyuzhuang Formation can be up to ~5 cm in width and can extend to over 20 cm in length, significantly exceeding the millimeter to centimeter-scale cracks commonly generated by wave loading (Forristall and Reece, 1985), as well as the scale of microcracks formed during conversion of smectite to illite (Meng et al., 2021).

Despite the lack of direct evidence, a gas generation and migration model has generally been considered to be the most plausible mechanism for the formation of MTS voids (Frank and Lyons, 1998; Furniss et al., 1998; Pollock et al., 2006; Shen et al., 2016). This model best explains the wide range of void morphologies and also provides a mechanism for void generation in shallow sediments near the SWI, which is consistent with the inferred environments and timing of MTS formation (Kriscautzky et al., 2022). The void morphologies are likely to be controlled by gas pressure and microscale gas-sediment interactions, with low gas production resulting in the spheroidal void morphologies and gradually increased gas production resulting in thin sinuous to thick ribbons during gas migration (Pollock et al., 2006). Our observations for the MTS from Member III of the Gaoyuzhuang Formation (Fig. 2), including the restriction of MTS to fine-grained micritic carbonates, a large number of co-occurring MTS morphologies within the same substrate, and the absence of detrital component infill of molar tooth microspar, are consistent with a comprehensive investigation of globally distributed MTS spanning different geological time periods (Pollock et al., 2006; Kuang, 2014; Hodgskiss et al., 2018; Kriscautzky et al., 2022). Hence, the gas expansion and migration model appears to be the most likely mechanism for the formation of MTS in the Gaoyuzhuang Formation. This model is also supported by a simulation experiment of gas generation and escape in a clay matrix, which reproduced the ribbon and blob-like voids that resemble the typical morphology of MTS (Furniss et al., 1998). In addition, voids similar to some MTS morphologies have also been found in modern freshwater sediments in association with gas production and effusion (e.g., Miller et al., 2018).

353 A variety of gases responsible for the formation of MTS have been proposed, including
354 H_2S associated with microbial sulfate reduction (Furniss et al., 1998), CO_2 associated with
355 the microbial oxidation of organic matter (Furniss et al., 1998) or destabilization of CO_2
356 clathrates within the sedimentary substrate (Marshall and Anglin, 2004), and CH_4
357 associated with methanogenesis (Shen et al., 2016). It is generally thought that the vast
358 majority of these gases responsible for the MTS formation are associated with microbial
359 activity near the SWI within the shallow substrate (Frank and Lyons 1998, Furniss et al.,
360 1998; Shen et al., 2016). We explore these potential microbial processes in further detail
361 below.

362 **5.3 The role of biogeochemical processes in the formation of MTS**

363 Microbial sulfate reduction (MSR) has been invoked for driving MTS formation because
364 it can generate H_2S gas that may create voids within the sediment, and MSR can also
365 elevate porewater alkalinity triggering carbonate precipitation (Frank and Lyons, 1998;
366 Pollock et al., 2006; Shen et al., 2016). However, MSR is unlikely to be responsible for the
367 formation of MTS voids, because the inferred low sulfate concentration in the
368 Mesoproterozoic ocean (Kah et al., 2004; Luo et al., 2015; Fakhraee et al., 2019) would
369 hinder generation of sufficient H_2S to create voids within the substrate. This is supported
370 by the low pyrite content (<142 ppm) of our samples and equally low pyrite contents (~0.01
371 wt%) observed in a global MTS-bulk rock sample suite (Hodgskiss et al., 2018). However,
372 MSR may have contributed to the increase in local alkalinity in porewaters, helping to
373 trigger the precipitation of molar tooth microspar.

374 The marginally elevated $\delta^{34}S_{CAS}$ values (13.7 ± 2.7‰) of MTS compared to host rocks

375 (12.4 ± 0.7‰) suggests that molar tooth microspar was precipitated in the sulfate reduction
376 zone within the sediment column, because sulfate reduction would preferentially remove
377 ^{32}S from the porewater sulfate pool, leaving the residual sulfate pool enriched in ^{34}S
378 (Habicht and Canfield, 1997). This is also consistent with generally lower CAS
379 concentrations in MTS (57 ± 34 ppm) than in host rocks (94 ± 68 ppm). Although pyrite
380 grains were rare in our samples, the sporadic occurrence of diagenetic pyrite in MTS (Fig.
381 2) may reflect the generation of H_2S in porewater as a result of MSR.

382 The role of MSR in the formation of MTS is theoretically testable by considering the
383 carbon isotope composition of MTS, because MSR produces dissolved inorganic carbon
384 (DIC) enriched in ^{12}C, and thus subsequent carbonate precipitation is generally
385 characterized by low $\delta^{13}C$ values (Irwin et al., 1977). However, consistent with observations
386 from previous studies (Frank and Lyons, 1998; Hodgskiss et al., 2018), the $\delta^{13}C$
387 compositions of MTS (−0.3 ± 0.4‰) and host rocks (−0.1 ± 0.3‰) from the Gaoyuzhuang
388 Formation are very similar (Fig. 5), with a negligible difference in $\delta^{13}C$ ($\Delta^{13}C_{HR\text{-}MTS}$ = 0.1 ±
389 0.5‰) in matrix-MTS pairs (Fig. 6). Indeed, a $\delta^{13}C$ compilation (Supplementary Table S2)
390 of globally-distributed MTS and associated host rocks (Fig. 7) shows that the MTS values
391 fall within the range of contemporaneous seawater (Kah et al., 1999; Halverson et al., 2010;
392 Lyons et al., 2014), suggesting that MTS record the $\delta^{13}C$ composition of coeval seawater.
393 The lack of difference in $\delta^{13}C$ composition between MTS and host rocks has been
394 interpreted to reflect a large ambient marine DIC reservoir (and thus elevated carbonate
395 saturation) during the Precambrian, which may have obscured the ^{13}C-depleted isotopic
396 signal that would be expected from sulfate reduction (Frank and Lyons, 1998; Bartley and

Kah, 2004). It seems unlikely that CO_2 degassing during either microbial oxidation of organic matter or CO_2 clathrate decomposition is responsible for the formation of MTS, because both increased CO_2 partial pressure and bacterial fermentation tends to lower porewater pH, favoring calcite dissolution rather than precipitation.

Methanogenesis has been considered to be an important biogeochemical process in the formation of MTS, as evidenced by a slight enrichment of 0.5–1.0‰ in $\delta^{13}C$ of MTS relative to the host rock (Shen et al., 2016; Tang et al., 2023). In most cases, however, the $\delta^{13}C$ data presented here and from an extensive MTS sample set on a global scale show no clear difference in $\delta^{13}C$ between MTS and host rocks (Frank and Lyons, 1998; Hodgskiss et al., 2018). One possible explanation is that the $\delta^{13}C$ value of seawater DIC may have increased due to photosynthesis in the water column (Thompson et al., 1997), resulting in the measured $\delta^{13}C$ values of host rocks being higher than that of seawater (Tang et al., 2023). Alternatively, the similarity in $\delta^{13}C$ values between MTS and host rocks could be attributed to the buffering effect of a large marine DIC reservoir, masking the ^{13}C-enriched isotopic signal that would be expected from methanogenesis.

A recent study suggests that MTS may have formed in a MSR-methanogenesis convergence zone in sediments deposited under euxinic (sulfidic) bottom water conditions, where the voids were formed by methane production as a result of methanogenesis, with subsequent precipitation of carbonate minerals due to MSR (Shen et al., 2016). This model implies that MSR plays a primary role in the formation of MTS as evidenced by unusually high bulk rock pyrite contents of 0.05–1.37 wt%, with an average of 0.42 wt% (Shen et al., 2016). However, this is not the case for MTS in the Gaoyuzhuang Formation, since low

419 pyrite contents in both MTS and host rocks suggests a limited contribution from MSR.
420 Furthermore, multiple lines of evidence suggest that the Gaoyuzhuang Formation was
421 deposited under dominantly ferruginous conditions with pulsed oxygenation events (Luo et
422 al., 2021; Zhang et al., 2018). Although euxinia may have been particularly prevalent at
423 mid-depths along productive continental margins during the mid-Proterozoic (Planavsky et
424 al., 2011; Poulton and Canfield, 2011; Poulton et al., 2010), iron speciation data indicate
425 that at least some MTS-bearing rocks may have been formed under ferruginous water
426 column conditions (Sperling et al., 2013). Furthermore, MTS commonly occur in shallow
427 water carbonates where euxinia was rare (Hodgskiss et al., 2018). Indeed, there is a major
428 peak in the occurrence of MTS during the early Neoproterozoic (Fig. 7), coincident with a
429 transition to near-global ferruginous conditions (Guilbaud et al., 2015).

430 Recent carbonate iodine data from MTS and host rocks in the Gaoyuzhuang Formation
431 suggest that MTS may have been formed through mixing of anoxic porewater with
432 overlying moderately oxygenated seawater (Tang et al., 2023). The low Mn concentrations
433 in host rocks would then probably result from oxidative removal of Mn^{2+} from the water
434 column (Tang et al., 2023). This is consistent with the generally low Mn concentrations
435 (<150 ppm) we observed in host rock samples from Member III of the Gaoyuzhuang
436 Formation, which are similar to that preserved within other Mesoproterozoic carbonate
437 rocks deposited under dominantly oxic conditions (Kah et al., 2012; Gilleaudeau and Kah,
438 2013). In the Mesoproterozoic to early Neoproterozoic oceans with generally low oxygen
439 levels (Lyons et al., 2014), oxygen concentrations would have decreased rapidly within the
440 upper few millimeters of the sediment column, resulting in anoxic porewaters (Kriscautzky

et al., 2022). This is consistent with the occasional occurrence of pyrite in our MTS samples (Fig. 2), suggesting anoxic porewater conditions. In addition, the only slightly higher $\delta^{34}S$ values of pyrite in MTS (10.6 ± 1.5‰) relative to host rocks (9.5 ± 1.1‰) suggests a more limited sulfate pool in porewaters, but strongly buffered by seawater. Anoxic conditions and depleted sulfate in porewaters could have driven methanogenesis as a primary metabolic pathway.

In light of these observations, methanogenesis appears likely to have played a major role in the formation of voids in unlithified sediments, while molar tooth microspar was likely formed during seawater-buffered diagenesis in the sulfate reduction zone within the sediment column. Seawater-buffered diagenesis requires persistent intrusion of seawater into permeable sediments, which commonly occurs on shallow-water carbonate platforms, and this may have maintained porewater $\delta^{13}C_{DIC}$ close to seawater $\delta^{13}C_{DIC}$ (Hoffman and Lamothe, 2019). The similar $\delta^{13}C$ values between host rocks and MTS observed both in our samples and in globally-distributed MTS (Fig. 7) suggests that diagenetic fluids were strongly buffered by seawater, which would be as expected near the SWI. Furthermore, MTS and host rocks have similar minimum $^{87}Sr/^{86}Sr$ ratios (0.70524 and 0.70539, respectively), which are close to the Sr isotope ratio (~0.705) of Mesoproterozoic seawater (Fig. 5, Chen et al., 2022; Shields and Veizer, 2002). In addition, the $\delta^{34}S_{CAS}$ values for MTS (13.7 ± 2.7‰) are close to those of the host rocks (12.4 ± 0.7‰), which are similar to previously reported $\delta^{34}S_{CAS}$ values for Member III of the Gaoyuzhuang carbonates, with averages of 13.0 ± 1.8‰ (Luo et al., 2015) and 12.4‰ (Guo et al., 2015) in the Pingquan section, and 14.3‰ (Ma et al., 2023) in the Kuancheng section. These values fall within

463 the range of $\delta^{34}S_{CAS}$ estimates (14.7 ± 3.6‰) for global seawater at ~1.5−1.6 Ga (Fig. 5,
464 Luo et al., 2015), supporting a seawater-buffered chemistry for the molar tooth microspar.

465 **5.4 Links between marine sulfate concentration and MTS formation**

466 We propose here that marine sulfate concentrations likely exerted a major control on the
467 formation of MTS. Methanogenesis would have been particularly important under low
468 sulfate conditions (Habicht et al., 2002; Pavlov et al., 2003), and the consequent methane
469 production and migration likely created significant void space for MTS formation. This
470 appears to have been the case for the Mesoproterozoic Gaoyuzhuang Formation, whereby
471 relatively higher $\delta^{34}S_{Py}$ values coupled with low pyrite contents indicate near quantitative
472 sulfate reduction from a small seawater sulfate reservoir. Sulfur isotope fractionations
473 between seawater sulfate and pyrite ($\Delta^{34}S_{CAS\text{-}Py}$) of 4.1 ± 1.5‰ in our host rock samples
474 from Member III of the Gaoyuzhuang Formation are comparable to previously reported
475 data (5.4 ± 1.4‰) (Fig. 5), which yielded a modelled seawater sulfate concentration
476 estimate of <0.1−0.35 mM (Luo et al., 2015). These sub-millimolar seawater sulfate
477 concentrations inferred from the Gaoyuzhuang Formation are also more broadly consistent
478 with previous estimates of <1 mM for the earliest Mesoproterozoic (Canfield et al., 2010;
479 Kah et al., 2004), and <0.4 mM for much of the Proterozoic (Fakhraee et al., 2019).
480 Furthermore, extensive MTS formation in the early Neoproterozoic occurred coincident
481 with the development of particularly low marine sulfate concentrations (estimated to be 0.8
482 ± 0.2 mM) from ~1.0−0.9 Ga (Guilbaud et al., 2015). Low oceanic sulfate concentrations
483 coincide with the widespread occurrence and elevated abundance of MTS (Fig. 7) through
484 the Mesoproterozoic and early Neoproterozoic (James et al., 1998; Kriscautzky et al.,

2022), suggesting that low seawater sulfate concentrations may have played a vital role in the formation of MTS. Indeed, voids similar to some MTS morphologies occur in modern freshwater sediments (Miller et al., 2018), where sulfate availability is generally limited (Lopes et al., 2011).

It is noteworthy that in some stratigraphic sections where MTS are developed, the beds with MTS are commonly interbedded with adjacent beds without MTS (Pollock et al., 2006; Mei and Tucker, 2011; Shen et al., 2016). The heterogeneity in MTS distribution within a given strata has also been documented in the Gaoyuzhuang Formation, and is considered to be controlled by sedimentary cycles, with MTS being rare and absent in more argillaceous deeper water sediments (Mei and Tucker, 2011). This is consistent with the environmental distribution of MTS, most of which appear in intertidal to shallow subtidal environments and are typically absent in deeper water settings (reviewed by Kuang, 2014; Kriscautzky et al., 2022). One possible explanation is that the local gas pressure resulting from methane production must be balanced by the hydrostatic pressure (which is dependent on water depth), and thus greater water depths are not conducive to the formation of cracks (Shen et al., 2016).

We also note that the coexistence of MTS and sulfate evaporites in some strata, such as the ~1.2 Ga carbonate-evaporite succession of the Society Cliffs Formation, northern Baffin and Bylot Islands (Kah et al., 2001), may argue against a role for low seawater sulfate concentrations in the formation of MTS. However, MTS and sulfate evaporites do not occur in the same stratigraphic interval in the Society Cliffs strata, and the carbonate facies of the interval containing MTS are significantly different from that of the interval

507 containing evaporites (Kah et al., 2001). Indeed, MTS are typically absent from evaporitic
508 settings (Bartley et al., 2000; Kah et al., 2001; Kriscautzky et al., 2022). In addition,
509 evaporite phases were not identified in our samples and there is no evidence of evaporites
510 in the Gaoyuzhuang Formation. Furthermore, on a microscopic scale, there is no clear
511 evidence that MTS diagenetically replaced evaporite minerals (Pratt, 1998; Bishop and
512 Sumner 2006), and molar tooth microspar lacks the petrographic characteristics of a
513 replacement mineral phase (Pollock et al., 2006). Given that the precise age of MTS and
514 relationships to potential short-term fluctuations in seawater sulfate concentrations are
515 poorly constrained, our model for MTS formation is not necessarily inconsistent with
516 observations of MTS and sulfate evaporites occurring in the same stratigraphic
517 successions.

518 We further propose a conceptual model to link low marine sulfate concentrations to MTS
519 formation. Marine sulfate concentrations play an important role in regulating the production
520 and benthic flux of methane in sediments (He et al., 2020). In Proterozoic oceans with
521 extremely low dissolved sulfate concentrations, available sulfate would have been rapidly
522 consumed by organic matter remineralization and sulfate reduction (Fakhraee et al., 2019;
523 Pavlov et al., 2003), ultimately leading to enhanced methane production. Anaerobic
524 oxidation of methane (AOM) would have been suppressed by the limited sulfate supply,
525 allowing methane to accumulate significantly in near-surface sediments, thus creating
526 voids close to the SWI during methane emission (Fig. 8). Furthermore, with regards to the
527 lack of AOM in sediments, the MTS would not be expected to show a $\delta^{13}C$ overprint from
528 extensive methane oxidation, even though the voids were generated by methane leakage.

On the other hand, the locally increased alkalinity in porewaters by MSR could have triggered the rapid precipitation of molar tooth microspar. The large DIC reservoir in Precambrian oceans (Bartley and Kah, 2004) would have additionally resulted in a small gradient in carbonate saturation between the water column and sediments, promoting rapid carbonate precipitation in the void spaces of unlithified sediments near the SWI (Higgins et al., 2009), where seawater-buffered diagenesis could have prevailed (Fig. 8).

The absence of MTS throughout most of the Palaeoproterozoic and after the mid-Neoproterozoic (Fig. 7) coincides with elevated seawater sulfate concentrations (Canfield and Farquhar, 2009; Fakhraee et al., 2019). Under higher seawater sulfate conditions, AOM would more effectively consume methane in the sulfate-methane transition zone, thereby limiting the accumulation of methane and preventing the generation of voids required for MTS formation. However, a seawater sulfate control does not explain the general lack of MTS in the Archean, which may instead be attributed to an overall low proportion of carbonate deposition (Cameron and Baumann, 1972; Cantine et al., 2020). Archean carbonates may have been mainly deposited in deeper ocean environments, due to the lack of an extensive stable continental shelf, and would have been removed from the geological record as a result of subduction of deep-ocean sediments (Cameron and Baumann, 1972). The size of the DIC reservoir and therefore the carbonate saturation state may also have played a role in the formation of MTS (Frank and Lyons, 1998; Bartley and Kah 2004; Pollock et al., 2006). Cohesive, yet unlithified, sediments were probably rarer in the Archean and Paleoproterozoic because elevated carbonate saturation would have resulted in rapid lithification of the substrate (Grotzinger, 1990, Cantine et al., 2020), which

likely prevented the formation of voids within the substrate (Pollock et al., 2006; Kriscautzky et al., 2022). By contrast, a continued decline in carbonate saturation after the mid-Neoproterozoic was likely insufficient to trigger rapid calcite microspar precipitation (Shields, 2002; Pollock et al., 2006; Hodgskiss et al., 2018).

The MTS record thus provides a potential archive of strong methane effluxes from sediments in low sulfate Proterozoic oceans. This is consistent with previous suggestions of large Proterozoic ocean methane fluxes of ~10–20 times the modern global flux (Fakhraee et al., 2019; Pavlov et al., 2003). Indeed, significant benthic methane fluxes from sediments may have played an important role in maintaining ice-free conditions and low oxygen levels throughout the Proterozoic (Fakhraee et al., 2019; Zhao et al., 2018).

6. Conclusions

Our study of MTS and associated carbonate matrix from the Mesoproterozoic Gaoyuzhuang Formation of the North China Craton supports a very early formation of MTS close to the SWI prior to sediment lithification and compaction. The C, S and Sr isotope signatures of MTS are close to those of host rocks, and are similar to the isotopic composition of contemporaneous global seawater, indicating a seawater-buffered diagenetic origin for MTS. Low $\Delta^{34}S_{CAS\text{-}Py}$ values in Gaoyuzhuang carbonates provide support for sub-millimolar sulfate concentrations in Mesoproterozoic seawater. In contrast to previous suggestions, our data therefore suggest a key role for oceanic sulfate levels in the formation of MTS. The temporal restriction of Proterozoic MTS broadly follows proposed changes in seawater sulfate concentrations, with low sulfate concentrations

occurring coincident with the widespread preservation of MTS during parts of the Mesoproterozoic to early Neoproterozoic. At very low seawater sulfate levels, limited AOM would have allowed methane to accumulate significantly, with voids subsequently created in unlithified sediments during benthic methane escape. These observations suggest that MTS likely provide a novel record of elevated methane fluxes from sediments.

Declaration of Competing Interest

The authors declare that they have no known competing financial interests or personal relationships that could have appeared to influence the work reported in this paper.

Acknowledgments

This work was supported by the National Natural Science Foundation of China (42102171, 41888101, 41927801), the Fundamental Research Funds for the Central Universities (3132023159). M.Z. is funded by the 100 Talents programme of the Chinese Academy of Sciences (E251520401) and the IGGCAS Key programme (no. IGGCAS-202201). S.W.P. acknowledges support from the Natural Environment Research Council (NE/R010129/01). We would like to thank Malcolm Hodgskiss, Linda Kah and an anonymous reviewer for their constructive and insightful comments that significantly improved the manuscript. We also thank Alexandra Turchyn and Jeffrey Catalano for their editorial input.

Appendix A. Supplementary Material

595

596 # References

597 Amarasinghe, U., Chaudhuri, A., Collins, A.S., Deb, G., Patranabis-Deb, S., 2015. Evolving provenance
598 in the Proterozoic Pranhita-Godavari Basin, India. Geosci. Front. 6, 453-463.

599 Banner, J.L., Hanson, G.N., 1990. Calculation of simultaneous isotopic and trace element variations
600 during waterrock interaction with applications to carbonate diagenesis. Geochim. Cosmochim. Acta
601 54, 3123-3137.

602 Bartley, J.K., Kah, L.C., 2004. Marine carbon reservoir, C_{org}-C_{carb} coupling, and the evolution of the
603 Proterozoic carbon cycle. Geology 32, 129-132.

604 Bishop, J.W., Sumner, D.Y., 2006. Molar tooth structures of the Neoarchean Monteville Formation,
605 Transvaal Supergroup, South Africa. I: Constraints on microcrystalline $CaCO_3$ precipitation.
606 Sedimentology 53, 1049-1068.

607 Blättler, C.L., Claire, M.W., Prave, A.R., Kirsimäe, K., Higgins, J.A., Medvedev, P.V., Romashkin, A.E.,
608 Rychanchik, D.V., Zerkle, A.L., Paiste, K., Kreitsmann, T., Millar, I.L., Hayles, J.A., Bao, H., Turchyn,
609 A.V., Warke, M.R., Lepland, A., 2018. Two-billion-year-old evaporites capture Earth's great
610 oxidation. Science 360, 320-323.

611 Brand, U., Veizer, J., 1980. Chemical diagenesis of a multicomponent carbonate system; 1, Trace
612 elements. J. Sediment. Petrol. 50, 1219-1236.

613 Cameron, E.M., Baumann, A., 1972. Carbonate sedimentation during the Archean. Chem. Geol. 10, 17-
614 30.

615 Canfield, D.E., Farquhar, J., 2009. Animal evolution, bioturbation, and the sulfate concentration of the
616 oceans. Proc. Natl. Acad. Sci. U. S. A. 106, 8123-8127.

617 Canfield, D.E., Farquhar, J., Zerkle, A.L., 2010. High isotope fractionations during sulfate reduction in a
618 low-sulfate euxinic ocean analog. Geology 38, 415-418.
619 Canfield, D.E., Raiswell, R., Westrich, J.T., Reaves, C.M., Berner, R.A., 1986. The Use of Chromium
620 Reduction in the Analysis of Reduced Inorganic Sulfur in Sediments and Shales. Chem. Geol. 54,
621 149-155.
622 Cantine, M.D., Knoll, A.H., Bergmann, K.D., 2020. Carbonates before skeletons: A database approach.
623 Earth Sci. Rev. 201, 103065.
624 Chen, X., Zhou, Y., Shields, G.A., 2022. Progress towards an improved Precambrian seawater $^{87}Sr/^{86}Sr$
625 curve. Earth Sci. Rev. 224, 103869.
626 Chu, X., Zhang, T., Zhang, Q., Lyons, T.W., 2007. Sulfur and carbon isotope records from 1700 to 800
627 Ma carbonates of the Jixian section, northern China: Implications for secular isotope variations in
628 Proterozoic seawater and relationships to global supercontinental events. Geochim. Cosmochim.
629 Acta 71, 4668-4692.
630 Evans, D.A.D., 2006. Proterozoic low orbital obliquity and axial-dipolar geomagnetic field from evaporite
631 palaeolatitudes. Nature 444, 51-55.
632 Fakhraee, M., Crowe, S.A., Katsev, S., 2018. Sedimentary sulfur isotopes and Neoarchean ocean
633 oxygenation. Sci. Adv. 4, e1701835.
634 Fakhraee, M., Hancisse, O., Canfield, D.E., Crowe, S.A., Katsev, S., 2019. Proterozoic seawater sulfate
635 scarcity and the evolution of ocean-atmosphere chemistry. Nat. Geosci. 12, 375-380.
636 Fike D. A., Bradley A. S. and Rose C. V., 2015. Rethinking the ancient sulfur cycle. Annu. Rev. Earth Pl.
637 Sc. 43, 593-622.
638 Fichtner, V., Strauss, H., Immenhauser, A., Buhl, D., Neuser, R.D., Niedermayr, A., 2017. Diagenesis of

639 carbonate associated sulfate. Chem. Geol. 463, 61-75.
640 Forristall, G.Z., Reece, A.M., 1985. Measurements of Wave Attenuation Due to a Soft Bottom-the
641 Swamp Experiment. J Geophys Res-Oceans 90, 3367-3380.
642 Frank, T.D., Lyons, T.W., 1998. "Molar-tooth" structures: A geochemical perspective on a Proterozoic
643 enigma. Geology 26, 683-686.
644 Furniss, G., Rittel, J.F., Winston, D., 1998. Gas bubble and expansion crack origin of "molar-tooth"
645 calcite structures in the Middle Proterozoic Belt Supergroup, western Montana. J. Sediment. Res.
646 68, 104-114.
647 Gill, B.C., Lyons, T.W., Frank, T.D., 2008. Behavior of carbonate-associated sulfateduring meteoric
648 diagenesis and implications for the sulfur isotope paleoproxy. Geochim. Cosmochim. Acta 72,
649 4699-4711.
650 Gilleaudeau, G.J., Kah, L.C., 2013. Carbon isotope records in a Mesoproterozoic epicratonic sea:
651 carbon cycling in a low-oxygen world. Precambrian Res. 228, 85-101.
652 Grotzinger, J.P., 1990. Geochemical Model for Proterozoic Stromatolite Decline. Am. J. Sci. 290a, 80-
653 103.
654 Guilbaud, R., Poulton, S.W., Butterfield, N.J., Zhu, M.Y., Shields-Zhou, G.A., 2015. A global transition
655 to ferruginous conditions in the early Neoproterozoic oceans. Nat. Geosci. 8, 466-470.
656 Guo, H., Du, Y., Kah, L.C., Hu, C., Huang, J., Huang, H., Yu, W., Song, H., 2015. Sulfur isotope
657 composition of carbonate-associated sulfate from the Mesoproterozoic Jixian Group, North China:
658 Implications for the marine sulfur cycle. Precambrian Res. 266, 319-336.
659 Habicht, K.S., Canfield, D.E., 1997. Sulfur isotope fractionation during bacterial sulfate reduction in
660 organic-rich sediments. Geochim. Cosmochim. Acta 61, 5351-5361.

661 Habicht, K.S., Gade, M., Thamdrup, B., Berg, P., Canfield, D.E., 2002. Calibration of sulfate levels in
662 the Archean Ocean. Science 298, 2372-2374.
663 Halverson, G.P., Wade, B.P., Hurtgen, M.T., Barovich, K.M., 2010. Neoproterozoic chemostratigraphy.
664 Precambrian Res. 182, 337-350.
665 He, T., Corso, J.D., Newton, R.J., Wignall, P.B., Mills, B.J.W., Todaro, S., Stefano, P.D., Turner, E.C.,
666 Jamieson, R.A., Randazzo, V., Rigo, M., Jones, R.E., Dunhill, A.M., 2020. An enormous sulfur
667 isotope excursion indicates marine anoxia during the end-Triassic mass extinction. Sci. Adv. 6,
668 eabb6704.
669 He, T.-C., Zhu, M.-Y., Mills, B.J.W., Wynn, P.M., Zhuravlev, A.Y., Tostevin, R., von Strandmann, P.A.E.P.,
670 Yang, A.H., Poulton, S.W., Shields, G.A., 2019. Possible links between extreme oxygen
671 perturbations and the Cambrian radiation of animals. Nat. Geosci. 12, 468-474.
672 Higgins, J.A., Fischer, W.W., Schrag, D.P., 2009. Oxygenation of the ocean and sediments:
673 Consequences for the seafloor carbonate factory. Earth Planet. Sci. Lett. 284, 25-33.
674 Hodgskiss, M.S.W., Kunzmann, M., Poirier, A., Halverson, G.P., 2018. The role of microbial iron
675 reduction in the formation of Proterozoic molar tooth structures. Earth Planet. Sci. Lett. 482, 1-11.
676 Hoffman, P.F., Lamothe, K.G., 2019. Seawater-buffered diagenesis, destruction of carbon isotope
677 excursions, and the composition of DIC in Neoproterozoic oceans. Proc. Natl. Acad. Sci. U. S. A.
678 116, 18874-18879.
679 Irwin, H., Curtis, C., Coleman, M., 1977. Isotopic evidence for source of diagenetic carbonates formed
680 during burial of organic-rich sediments. Nature 269, 209-213.
681 James, N.P., Narbonne, G.M., Sherman, A.G., 1998. Molar-tooth carbonates: Shallow subtidal facies of
682 the mid-to late Proterozoic. J. Sediment. Res. 68, 716-722.

683 Kah, L.C., Bartley, J.K., 2022. Carbonate fabric diversity and environmental heterogeneity in the late
684 Mesoproterozoic Era. Geol. Mag. 159, 220-46.
685 Kah, L.C., Bartley, J.K., Teal, D.A., 2012. Chemostratigraphy of the Late Mesoproterozoic Atar Group,
686 Taoudeni Basin, Mauritania: muted isotopic variability, facies correlation, and global isotopic trends.
687 Precambrian Res. 200-203, 82-103.
688 Kah, L.C., Lyons, T.W., Chesley, J.T., 2001. Geochemistry of a 1.2 Ga carbonate-evaporite succession,
689 northern Baffin and Bylot Islands: implications for Mesoproterozoic marine evolution. Precambrian
690 Res. 111:203–234.
691 Kah, L.C., Lyons, T.W., Frank, T.D., 2004. Low marine sulphate and protracted oxygenation of the
692 proterozoic biosphere. Nature 431, 834-838.
693 Kah, L.C., Sherman, A.G., Narbonne, G.M., Knoll, A.H., Kaufman, A.J., 1999. $\delta^{13}C$ isotope stratigraphy
694 of the Mesoproterozoic Bylot Supergroup, northern Baffin Island: implications for regional
695 lithostratigraphic correlations. Can. J. Earth Sci. 36, 313-332.
696 Kaufman, A.J., Jacobsen, S.B., Knoll, A.H., 1993. The Vendian Record of Sr and C-Isotopic Variations
697 in Seawater-Implications for Tectonics and Paleoclimate. Earth Planet. Sci. Lett. 120, 409-430.
698 Kriscautzky, A., Kah, L. C., Bartley, J. K. 2022. Molar-Tooth Structure as a window into the deposition
699 and diagenesis of Precambrian carbonate. Annu. Rev. Earth Planet. Sci. 50, 205-230.
700 Kuang, H.W., 2014. Review of molar tooth structure research. J. Palaeogeogr. 3, 359-383.
701 Land, L.S., 1980. The Isotopic and Trace Element Geochemistry of Dolomite: The State of the Art. In:
702 Zenger D. H., Dunham J. B., Ethington R. L.(Eds.), Concepts and Models of Dolomitization. Society
703 for Sedimentary Geology, pp. 87-110.
704 Li, C., Planavsky, N.J., Love, G.D., Reinhard, C.T., Hardisty, D., Feng, L.-J., Bates, S.M., Huang, J.,

705 Zhang, Q.R., Chu, X.-L., Lyons, T.W., 2015. Marine redox conditions in the middle Proterozoic
706 ocean and isotopic constraints on authigenic carbonate formation: Insights from the Chuanlinggou
707 Formation, Yanshan Basin, North China. Geochim. Cosmochim. Acta 150, 90-105.
708 Li, D., Shields-Zhou, G.A., Ling, H.F., Thirlwall, M., 2011. Dissolution methods for strontium isotope
709 stratigraphy: Guidelines for the use of bulk carbonate and phosphorite rocks. Chem. Geol. 290,
710 133-144.
711 Li, H.-K., Su, W.-B., Zhou, H.-Y., Xiang, Z.-Q., Tian, H., Yang, L.-G., Huff, W.D., Ettensohn, F.R., 2014.
712 The first precise age constraints on the Jixian System of the Meso- to Neoproterozoic Standard
713 Section of China: SHRIMP zircon U-Pb dating of bentonites from the Wumishan and Tieling
714 formations in the Jixian Section, North China Craton. Acta Petrol Sin 30, 2999-3012.
715 Li, H.-K., Zhu, S.-X., Xiang, Z.-Q., Su, W.-B., Lu, S.-N., Zhou, H.-Y., Geng, J.-Z., Li, S., Yang, F.-J., 2010.
716 Zircon U-Pb dating on tuff bed from Gaoyuzhuang Formation in Yanqing, Beijing: Further
717 constraints on the new subdivision of the Mesoproterozoic stratigraphy in the northern North China
718 Craton. Acta Petrol Sin 26, 2131-2140.
719 Lopes, F., Viollier, E., Thiam, A., Michard, G., Abril, G., Groleau, A., Prevot, F., Carrias, J.F., Alberic, P.,
720 Jezequel, D., 2011. Biogeochemical modelling of anaerobic vs. aerobic methane oxidation in a
721 meromictic crater lake (Lake Pavin, France). Appl. Geochem. 26, 1919-1932.
722 Lu, S., Zhao, G., Wang, H., Hao, G., 2008. Precambrian metamorphic basement and sedimentary cover
723 of the North China Craton: a review. Precambrian Res. 160, 77-93.
724 Luo, G.-M., Ono, S.H., Huang, J.-H., Algeo, T.J., Li, C., Zhou, L., Robinson, A., Lyons, T.W., Xie, S.C.,
725 2015. Decline in oceanic sulfate levels during the early Mesoproterozoic. Precambrian Res. 258,
726 36-47.

727 Luo, J., Long, X., Bowyer, F.T., Mills, B.J., Li, J., Xiong, Y., Zhu, X., Zhang, K., Poulton, S.W., 2021.
728 Pulsed oxygenation events drove progressive oxygenation of the early Mesoproterozoic ocean.
729 Earth Planet. Sci. Lett. 559, 116754.
730 Lyons T. W., Hurtgen M. T. and Gill B. C. (2005) New insight into the utility of carbonate-associated
731 sulfate. Geochim. Cosmochim. Acta 69, A128.
732 Lyons, T.W., Reinhard, C.T., Planavsky, N.J., 2014. The rise of oxygen in Earth's early ocean and
733 atmosphere. Nature 506, 307-315.
734 Ma, P., Guo, H.F., Du, Y., Yu, W., Jin, S., Xu, L., 2023. Dynamic seawater redox status in the early
735 Mesoproterozoic: Evidence from trace elements and sulfur isotopic compositions of carbonate
736 associated sulfate in multiple sections. Precambrian Res. 385, 106953.
737 Marenco, P.J., Corsetti, F.A., Hammond, D., Kaufman, A.J., Bottjer, D.J., 2008. Oxidation of pyrite during
738 extraction of carbonate associated sulfate. Chem. Geol. 247, 124-132.
739 Marshall, D., Anglin, C., 2004. CO2-clathrate destabilization: a new model of formation for molar tooth
740 structures. Precambrian Res. 129, 325-341.
741 Mazumdar, A., Goldberg, T., Strauss, H., 2008. Abiotic oxidation of pyrite by Fe(III. in acidic media and
742 its implications for sulfur isotope measurements of lattice-bound sulfate in sediments. Chem. Geol.
743 253, 30-37.
744 McArthur, J., Howarth, R., Shields, G., 2012. Strontium isotope stratigraphy. In: Gradstein F. M., Ogg J.
745 G., Schmitz M. D., Ogg G. M.(Eds.), The Geologic Time Scale. Elsevier, Boston, pp. 127-144.
746 Mei, M.X., Tucker, M.E., 2011. Molar Tooth Structure: a Contribution from the Mesoproterozoic
747 Gaoyuzhuang Formation, Tianjin City, North China. Acta Geol Sin-Engl 85, 1084-1099.
748 Meng, Q.F., Hao, F., Tian, J.Q., 2021. Origins of non-tectonic fractures in shale. Earth Sci. Rev. 222,

749 103825.
750 Miller, K., Simpson, E.L., Sherrod, L., Wizevich, M.C., Malenda, M., Morgano, K., Richardson, A.,
751 Livingston, K., Bogner, E., 2018. Gas bubble cavities in deltaic muds, Lake Powell delta, Glen
752 Canyon National Recreation Area, Hite, Utah. Mar. Pet. Geol. 92, 904-912.
753 Nier, A.O., 1938. The Isotopic Constitution of Strontium, Barium, Bismuth, Thallium and Mercury. Phys.
754 Rev. 54, 275-278.
755 Planavsky, N.J., McGoldrick, P., Scott, C.T., Li, C., Reinhard, C.T., Kelly, A.E., Chu, X.L., Bekker, A.,
756 Love, G.D., Lyons, T.W., 2011. Widespread iron-rich conditions in the mid-Proterozoic ocean.
757 Nature 477, 448-451.
758 Pollock, M. D., Kah, L. C., Bartley, J. K., 2006. Morphology of molar-tooth structures in precambrian
759 carbonates: Influence of substrate rheology and implications for genesis. J. Sediment. Res. 76,
760 310-323.
761 Poulton, S.W., Canfield, D.E., 2011. Ferruginous Conditions: A Dominant Feature of the Ocean through
762 Earth's History. Elements 7, 107-112.
763 Poulton, S.W., Fralick, P.W., Canfield, D.E., 2010. Spatial variability in oceanic redox structure 1.8 billion
764 years ago. Nat. Geosci. 3, 486-490.
765 Pratt, B. R., 1998. Molar-tooth structure in Proterozoic carbonate rocks: Origin from synsedimentary
766 earthquakes, and implications for the nature and evolution of basins and marine sediment. Geol.
767 Soc. Am. Bull. 110, 1028-1045.
768 Qiao, X.-F., Gao, L.-Z., 2007. Mesoproterozoic palaeoearthquake and palaeogeography in Yan-Liao
769 Aulacogen. J. Palaeogeogr. 9, 337-352.
770 Rennie, V.C., Turchyn, A.V., 2014. The preservation of and in carbonate-associated sulfate during

771 marine diagenesis: a 25 Myr test case using marine sediments. Earth Planet. Sci. Lett. 395, 13-23.
772 Shen, B., Dong, L., Xiao, S.-H., Lang, X.-G., Huang, K.-J., Peng, Y.-B., Zhou, C.-M., Ke, S., Liu, P.-J.,
773 2016. Molar tooth carbonates and benthic methane fluxes in Proterozoic oceans. Nat. Commun. 7,
774 10317.
775 Shields, G. A., 2002. 'Molar-tooth microspar': a chemical explanation for its disappearance similar to
776 750 Ma. Terra Nova 14, 108-113.
777 Shields, G., Veizer, J., 2002. Precambrian marine carbonate isotope database: Version 1.1. Geochem
778 Geophy Geosy 3, 1-12.
779 Sperling, E.A., Halverson, G.P., Knoll, A.H., Macdonald, F.A., Johnston, D.T., 2013. Abasin redox
780 transect at the dawn of animal life. Earth Planet. Sci. Lett. 371, 143-155.
781 Pavlov, A.A., Hurtgen, M.T., Kasting, J.F., Arthur, M.A., 2003. Methane-rich Proterozoic atmosphere?
782 Geology 31, 87-90.
783 Tang, D., Fang, H., Shi, X., Liang, L., Zhou, L., Xie, B., Huang, K., Zhou, X., Wu, M., Riding, R., 2023.
784 Mesoproterozoic Molar Tooth Structure Related to Increased Marine Oxygenation. J. Geophys. Res.
785 Biogeosci. 128, e2022JG007077.
786 Thompson, J. B., Schultze-Lam, S., Beveridge, T. J., Des Marais, D. J., 1997. Whiting events: Biogenic
787 origin due to the photosynthetic activity of cyanobacterial picoplankton. Limnol. Oceanogr. 42, 133-
788 141.
789 Tian, H., Zhang, J., Li, H.-K., Su, W.-B., Zhou, H.-Y., Yang, L.-G., Xiang, Z.-Q., Geng, J.-Z., Liu, H., Zhu,
790 S.-X., 2015. Zircon LA-MC-ICPMS U-Pb dating of tuff from Mesoproterozoic Gaoyuzhuang
791 Formation in Jixian County of North China and its geological significance. Acta Geosci. Sin. 36,
792 647-658.

793 Wang, X.-M., Zhang, S.-C., Wang, H.-J., Bjerrum, C.J., Hammarlund, E.U., Haxen, E.R., Su, J., Wang,
794 Y., Canfield, D.E., 2017. Oxygen, Climate and the Chemical Evolution of a 1400 Million Year Old
795 Tropical Marine Setting. Am. J. Sci. 317, 861-900.
796 Wotte, T., Shields-Zhou, G.A., Strauss, H., 2012. Carbonate-associated sulfate: Experimental
797 comparisons of common extraction methods and recommendations toward a standard analytical
798 protocol. Chem. Geol. 326, 132-144.
799 Zhang, K., Zhu, X.-K., Wood, R.A., Shi, Y., Gao, Z.-F., Poulton, S.W., 2018. Oxygenation of the
800 Mesoproterozoic ocean and the evolution of complex eukaryotes. Nat. Geosci. 11, 345-350.
801 Zhang, S., Wang, X., Wang, H., Bjerrum, C.J., Hammarlund, E.U., Costa, M.M., Connelly, J.N., Zhang,
802 B., Su, J., Canfield, D.E., 2016. Sufficient oxygen for animal respiration 1,400 million years ago.
803 Proc. Natl. Acad. Sci. 113, 1731-1736.
804
805
806 Figure captions
807 Figure 1. (a) The distribution of Proterozoic strata in the Yanliao aulacogen of the North
808 China Craton (Zhang et al., 2016), including the sampling location for the molar tooth
809 carbonates. (b) General stratigraphic column of the North China Craton (Wang et al., 2017)
810 and the detailed stratigraphic columns for Member III (Zhangjiayu member) of the
811 Gaoyuzhuang Formation.
812
813 Figure 2. (a) Outcrop photos showing molar tooth structures (black) in micritic limestone
814 (grey) from Member III of the Gaoyuzhuang Formation. (b) Photograph showing ribbon

815 molar tooth structures is connected to the bubble molar tooth structures. (c) and (d)
816 Photograph showing vertical ribbon molar tooth structures and horizontal banded molar
817 tooth structures. (e) Plan view of the bubble molar tooth structures. (f) Photograph showing
818 molar tooth microspar in a fine-grained host rock under transmitted light. (g) Photograph
819 showing the characteristic sharp boundary between molar tooth structures and micritic host
820 carbonate rocks under transmitted light. (h) Photograph showing the calcite microspar of
821 the molar tooth structures. (i) Photograph showing euhedral pyrite in the molar tooth
822 structures. Abbreviations: MTS, molar tooth structures; HR, host rocks; Py, pyrite.
823
824 Figure 3. (a) Crossplot of $\delta^{13}C$ versus Mn/Sr. (b) Crossplot of $\delta^{13}C$ versus $\delta^{18}O$. (c)
825 Crossplot of Mg/Ca versus Mn/Sr. (d) Crossplot of $\delta^{18}O$ versus Mg/Ca. Abbreviations: MTS,
826 molar tooth structures; HR, host rocks. No clear correlation is evident between $\delta^{18}O$ and
827 either $\delta^{13}C$ or Mg/Ca ratios, suggesting only limited diagenetic alteration or dolomitization.
828
829 Figure 4. (a) Crossplot of $\delta^{34}S_{CAS}$ versus Mn/Sr. (b) Crossplot of $\delta^{34}S_{CAS}$ versus Mg/Ca. (c)
830 Crossplot of $\delta^{34}S_{CAS}$ versus CAS concentrations. (d) Crossplot of $\delta^{34}S_{CAS}$ versus pyrite
831 contents. Abbreviations: MTS, molar tooth structures; HR, host rocks. No apparent
832 correlation between $\delta^{34}S_{CAS}$ and Mn/Sr, Mg/Ca ratio, CAS and pyrite concentration,
833 suggesting that diagenetic alteration and potential contamination from pyrite oxidation had
834 little impact on the isotopic composition of CAS.
835
836 Figure 5. Isotopic compositions of molar tooth structures and host rocks from Member III

of the Mesoproterozoic Gaoyuzhuang Formation. (a) $\delta^{13}C$ values, where the dotted line represents the average $\delta^{13}C$ value (~0‰) of the Mesoproterozoic Jixian Group (Chu et al., 2007). (b) $^{87}Sr/^{86}Sr$ values, where the dotted line represents the Sr isotope ratio (~0.705) of Mesoproterozoic seawater (Shields and Veizer, 2002; Chen et al., 2022). (c) S isotopic compositions of pyrite and CAS from molar tooth structures and host rocks. (d) Average S isotopic compositions of pyrite and CAS from molar tooth structures and host rocks and average $\Delta^{34}S_{CAS\text{-}Py}$ values based on paired sulfate and pyrite measurements. The average $^{34}S_{Py}$, $^{34}S_{CAS}$ and $\Delta^{34}S_{CAS\text{-}Py}$ values in the grey band represent previously reported data from Member III of the 1.56 Ga Gaoyuzhuang (GYZ) Formation and the compiled data from ~1.5−1.6 Ga (Luo et al., 2015, and references therein). Abbreviations: MTS, molar tooth structures; HR, host rocks.

Figure 6. Carbon isotope differences ($\Delta^{13}C_{HR\text{-}MTS}$) between paired host rock and molar tooth structures show a negligible difference in $\delta^{13}C$ ($\Delta^{13}C_{HR\text{-}MTS}$ = 0.1 ± 0.5‰) in matrix-MTS pairs. Abbreviations: MTS, molar tooth structures; HR, host rocks.

Figure 7. (a) Carbonate carbon isotope record through Earth history (Lyons et al., 2014) and compiled $\delta^{13}C$ data for molar tooth structures and associated host rocks. Black and red dots represent the $\delta^{13}C$ data of molar tooth structures and host rocks from the Gaoyuzhuang Formation, respectively. Grey and yellow dots represent the compiled $\delta^{13}C$ data from global molar tooth structures and associated host rocks, respectively (supplementary Table S2). (b) Histogram showing the distribution and abundance of molar

859 tooth structures through time (Kriscautzky et al., 2022), with the age of the Godavari
860 Supergroup, Gaoyuzhuang and Wumishan formations based on Amarasinghe et al. (2015),
861 Li et al. (2010, 2014), Tian et al. (2015). (c) Changes in oceanic sulfate concentration
862 through time. Dark grey band represents the estimated seawater sulfate concentration from
863 Fakhraee et al. (2018), green band represents the estimate from Fakhraee et al. (2019),
864 light grey band represents the estimate from Canfield and Farquhar (2009). Evaporite
865 depositional records from Evans (2006) and Blättler et al. (2018).
866
867 Figure 8. Conceptual model for molar tooth structures formation. (a) In Proterozoic oceans
868 with extremely low sulfate concentrations (<1 mM), sulfate would have been rapidly
869 consumed, restricting microbial sulfate reduction (MSR). Anaerobic oxidation of methane
870 (AOM) was suppressed by limited sulfate supply, and the methane produced by
871 methanogenesis could have accumulated and subsequently created voids during escape.
872 (b) The large dissolved inorganic carbon (DIC) reservoir in the Precambrian oceans
873 (Bartley and Kah, 2004) would have resulted in a small gradient in carbonate saturation
874 between the water column and host sediment, promoting rapid precipitation of carbonate
875 microspar in the void spaces of unlithified sediments near the SWI.
876
877 Table captions
878 Table 1. Comparison of geochemical signatures between MTS and host rock.
879
880

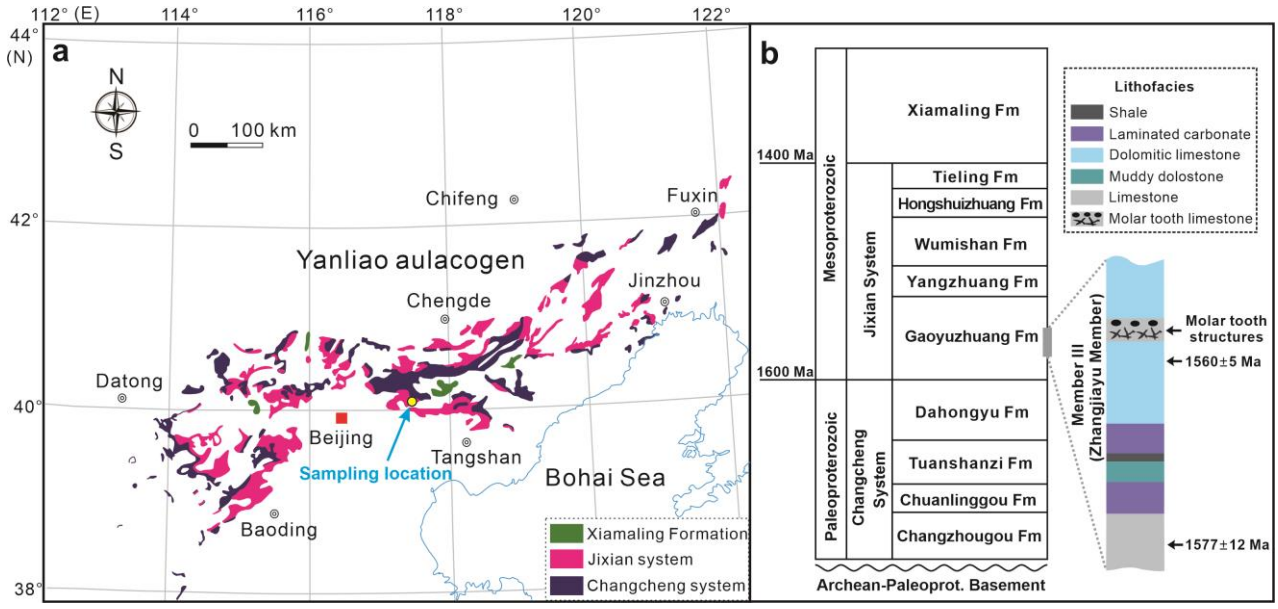

Figure 1. (a) The distribution of Proterozoic strata in the Yanliao aulacogen of the North China Craton (Zhang et al., 2016), including the sampling location for the molar tooth carbonates. (b) General stratigraphic column of the North China Craton (Wang et al., 2017) and the detailed stratigraphic columns for Member III (Zhangjiayu member) of the Gaoyuzhuang Formation.

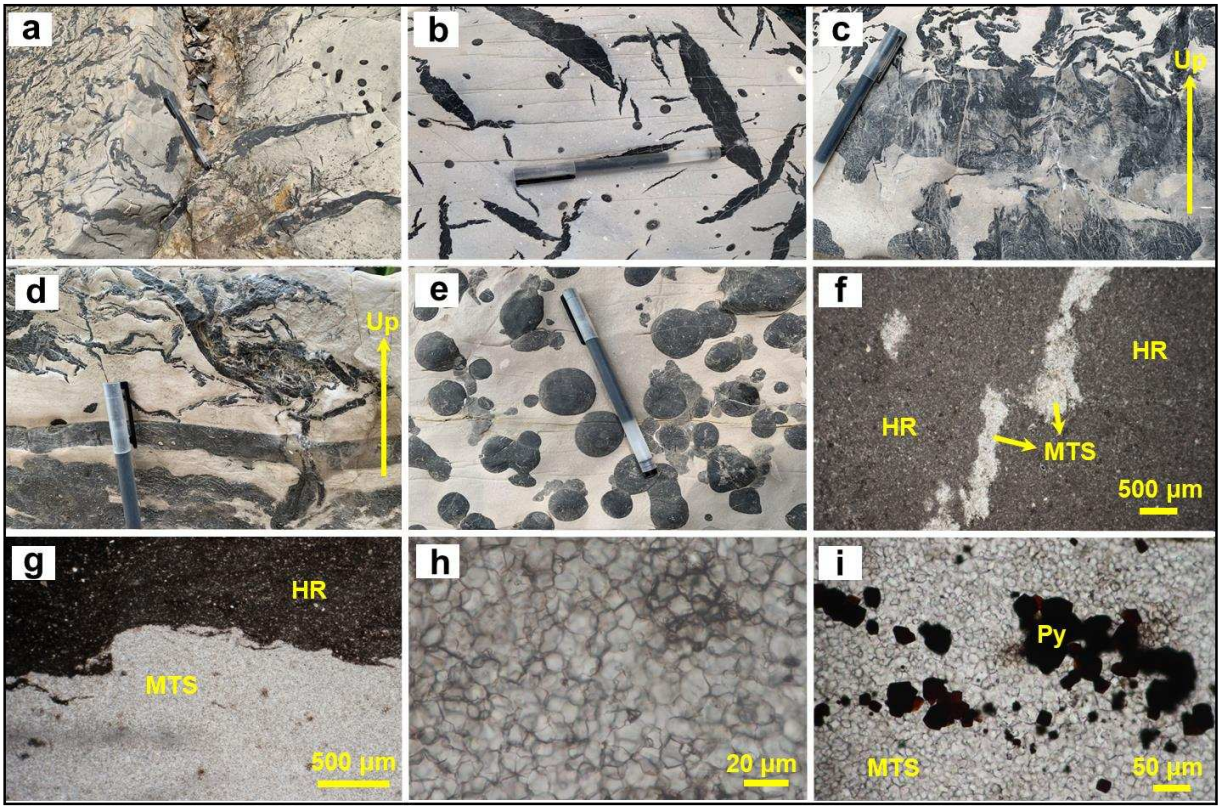

Figure 2. (a) Outcrop photos showing molar tooth structures (black) in micritic limestone (grey) from Member III of the Gaoyuzhuang Formation. (b) Photograph showing ribbon molar tooth structures is connected to the bubble molar tooth structures. (c) and (d) Photograph showing vertical ribbon molar tooth structures and horizontal banded molar tooth structures. (e) Plan view of the bubble molar tooth structures. (f) Photograph showing molar tooth microspar in a fine-grained host rock under transmitted light. (g) Photograph showing the characteristic sharp boundary between molar tooth structures and micritic host carbonate rocks under transmitted light. (h) Photograph showing the calcite microspar of the molar tooth structures. (i) Photograph showing euhedral pyrite in the molar tooth structures. Abbreviations: MTS, molar tooth structures; HR, host rocks; Py, pyrite.

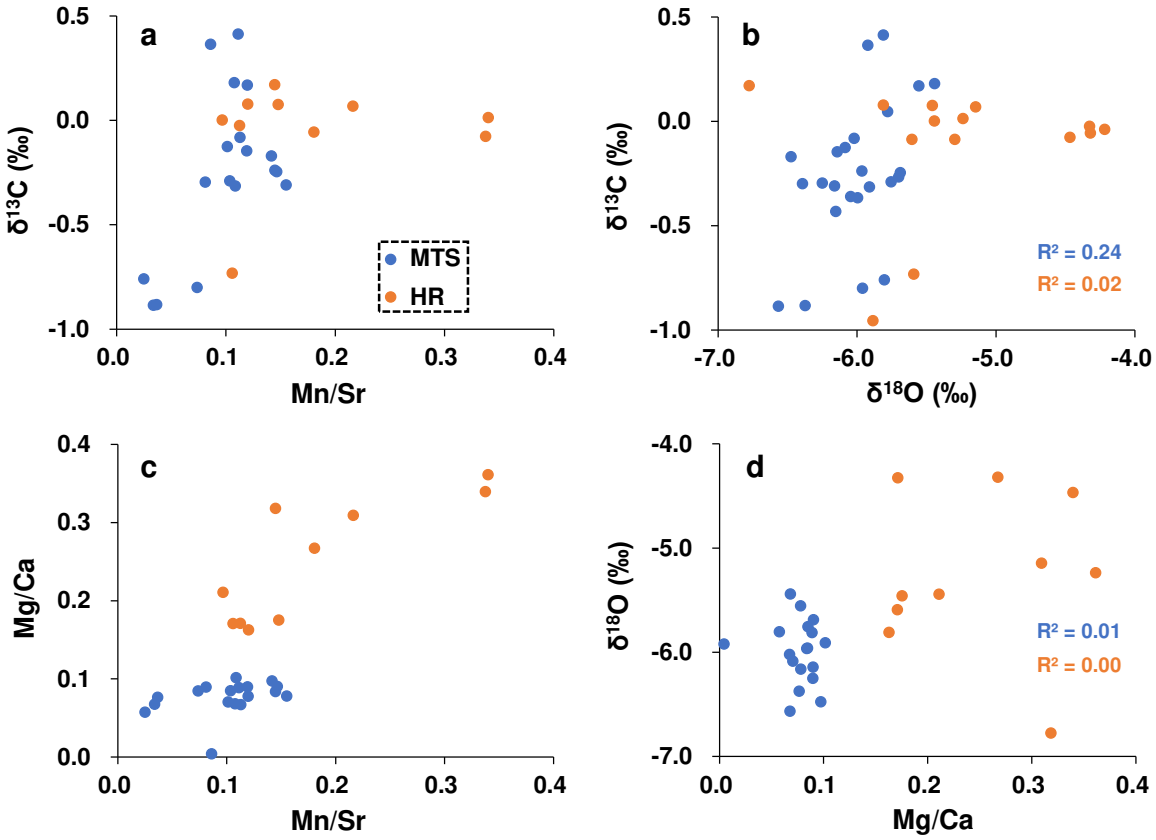

Figure 3. (a) Crossplot of $\delta^{13}C$ versus Mn/Sr. (b) Crossplot of $\delta^{13}C$ versus $\delta^{18}O$. (c) Crossplot of Mg/Ca versus Mn/Sr. (d) Crossplot of $\delta^{18}O$ versus Mg/Ca. Abbreviations: MTS, molar tooth structures; HR, host rocks. No clear correlation is evident between $\delta^{18}O$ and either $\delta^{13}C$ or Mg/Ca ratios, suggesting only limited diagenetic alteration or dolomitization.

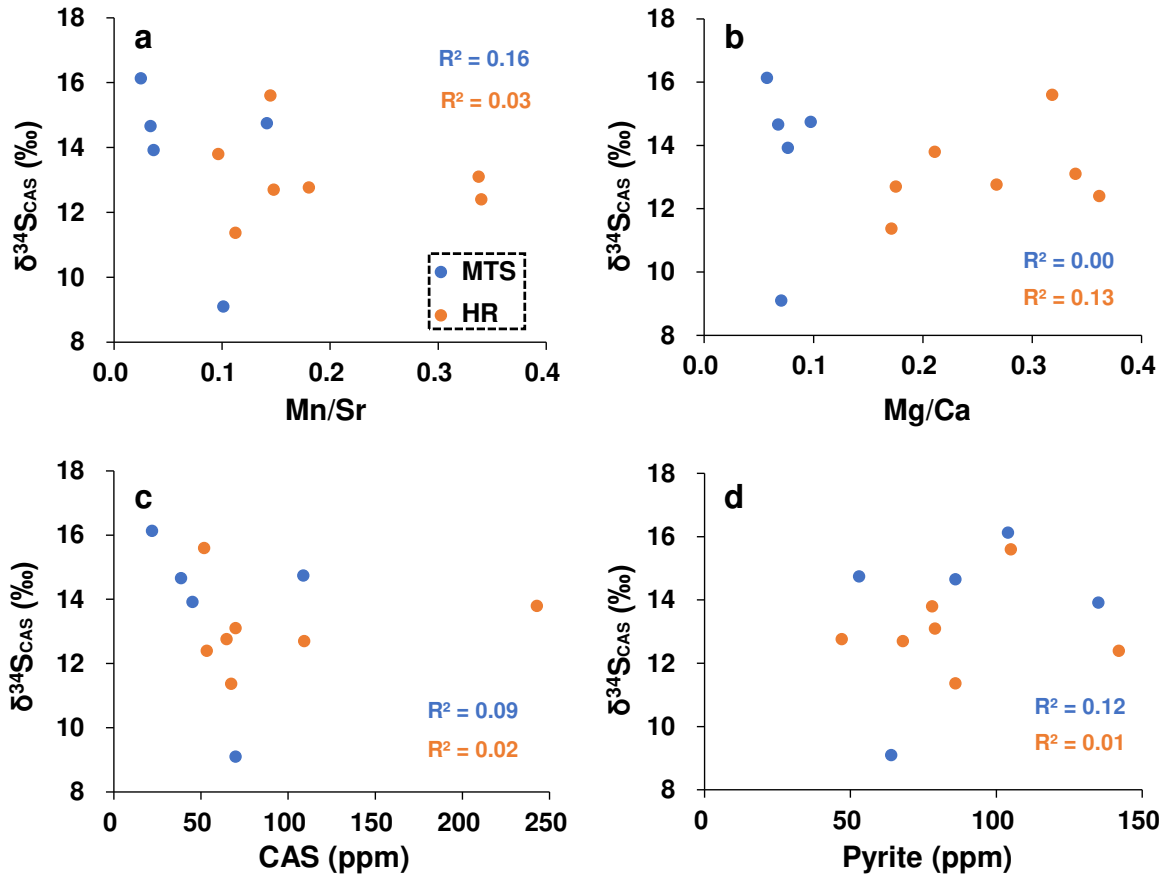

Figure 4. (a) Crossplot of $\delta^{34}S_{CAS}$ versus Mn/Sr. (b) Crossplot of $\delta^{34}S_{CAS}$ versus Mg/Ca. (c) Crossplot of $\delta^{34}S_{CAS}$ versus CAS concentrations. (d) Crossplot of $\delta^{34}S_{CAS}$ versus pyrite contents. Abbreviations: MTS, molar tooth structures; HR, host rocks. No apparent correlation between $\delta^{34}S_{CAS}$ and Mn/Sr, Mg/Ca ratio, CAS and pyrite concentration, suggesting that diagenetic alteration and potential contamination from pyrite oxidation had little impact on the isotopic composition of CAS.

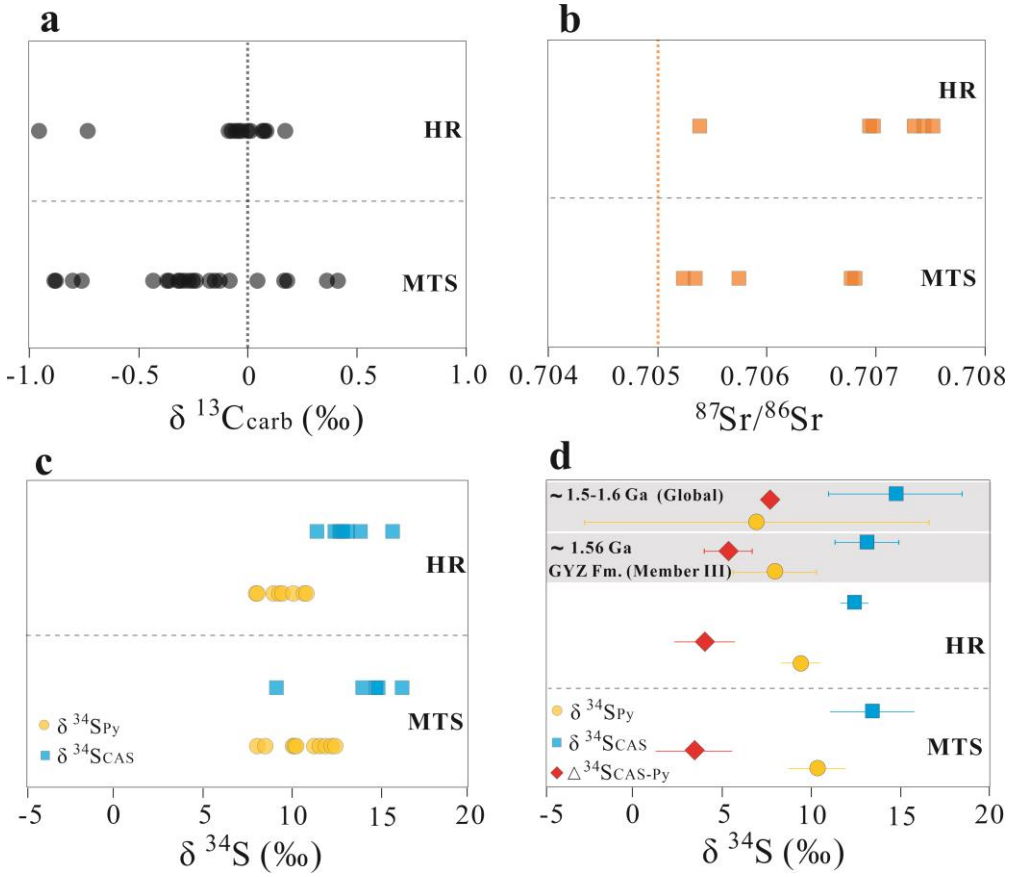

Figure 5. Isotopic compositions of molar tooth structures and host rocks from Member III of the Mesoproterozoic Gaoyuzhuang Formation. (a) $\delta^{13}C$ values, where the dotted line represents the average $\delta^{13}C$ value (~0‰) of the Mesoproterozoic Jixian Group (Chu et al., 2007). (b) $^{87}Sr/^{86}Sr$ values, where the dotted line represents the Sr isotope ratio (~0.705) of Mesoproterozoic seawater (Shields and Veizer, 2002; Chen et al., 2022). (c) S isotopic compositions of pyrite and CAS from molar tooth structures and host rocks. (d) Average S isotopic compositions of pyrite and CAS from molar tooth structures and host rocks and average $\Delta^{34}S_{CAS\text{-}Py}$ values based on paired sulfate and pyrite measurements. The average $^{34}S_{Py}$, $^{34}S_{CAS}$ and $\Delta^{34}S_{CAS\text{-}Py}$ values in the grey band represent previously reported data from Member III of the 1.56 Ga Gaoyuzhuang (GYZ) Formation and the compiled data from ~1.5−1.6 Ga (Luo et al., 2015, and references therein). Abbreviations: MTS, molar tooth structures; HR, host rocks.

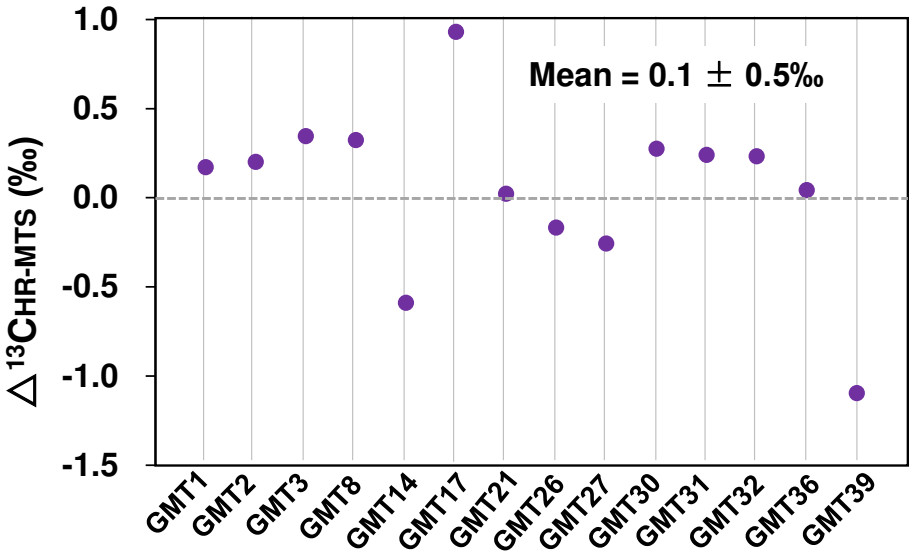

Figure 6. Carbon isotope differences ($\Delta^{13}C_{HR\text{-}MTS}$) between paired host rock and molar tooth structures show a negligible difference in $\delta^{13}C$ ($\Delta^{13}C_{HR\text{-}MTS}$ = 0.1 ± 0.5‰) in matrix-MTS pairs. Abbreviations: MTS, molar tooth structures; HR, host rocks.

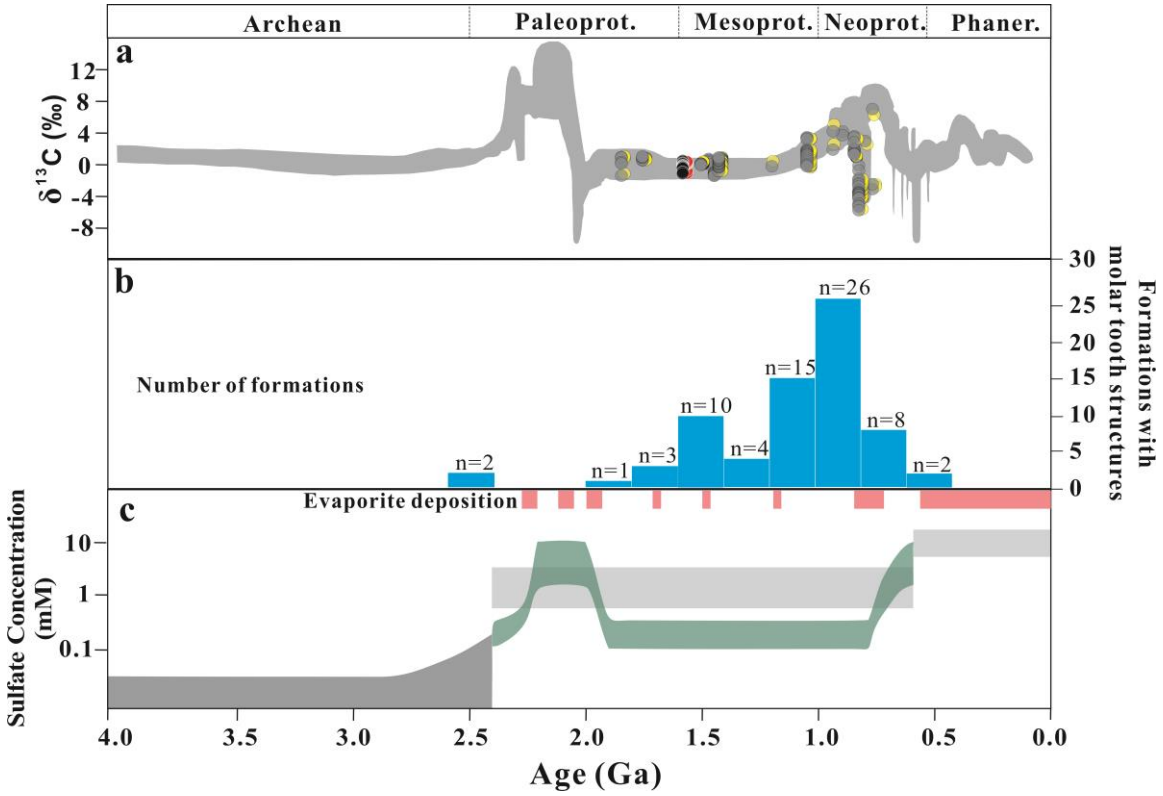

Figure 7. (a) Carbonate carbon isotope record through Earth history (Lyons et al., 2014) and compiled $\delta^{13}C$ data for molar tooth structures and associated host rocks. Black and red dots represent the $\delta^{13}C$ data of molar tooth structures and host rocks from the Gaoyuzhuang Formation, respectively. Grey and yellow dots represent the compiled $\delta^{13}C$ data from global molar tooth structures and associated host rocks, respectively (supplementary Table S2). (b) Histogram showing the distribution and abundance of molar tooth structures through time (Kriscautzky et al., 2022), with the age of the Godavari Supergroup, Gaoyuzhuang and Wumishan formations based on Amarasinghe et al. (2015), Li et al. (2010, 2014), Tian et al. (2015). (c) Changes in oceanic sulfate concentration through time. Dark grey band represents the estimated seawater sulfate concentration from Fakhraee et al. (2018), green band represents the estimate from Fakhraee et al. (2019), light grey band represents the estimate from Canfield and Farquhar (2009). Evaporite depositional records from Evans (2006) and Blättler et al. (2018).

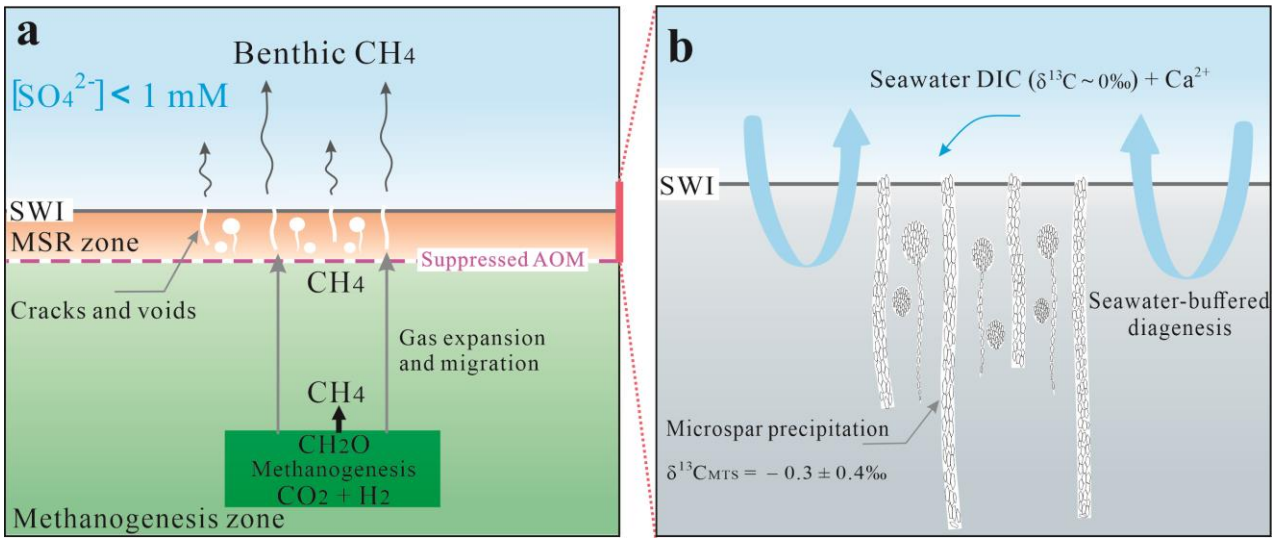

Figure 8. Conceptual model for molar tooth structures formation. (a) In Proterozoic oceans with extremely low sulfate concentrations (<1 mM), sulfate would have been rapidly consumed, restricting microbial sulfate reduction (MSR). Anaerobic oxidation of methane (AOM) was suppressed by limited sulfate supply, and the methane produced by methanogenesis could have accumulated and subsequently created voids during escape. (b) The large dissolved inorganic carbon (DIC) reservoir in the Precambrian oceans (Bartley and Kah, 2004) would have resulted in a small gradient in carbonate saturation between the water column and host sediment, promoting rapid precipitation of carbonate microspar in the void spaces of unlithified sediments near the SWI.

983

984 Table 1. Comparison of geochemical signatures between MTS and host rock.

Geochemical proxies	Difference between MTS and host rock	References
$\delta^{13}C$	Similar (~0‰)	This study, Frank and Lyons (1998), Hodgskiss et al. (2018)
	MTS > host rock (~0.5–1‰)	Shen et al. (2016), Tang et al. (2023)
$\delta^{18}O$	MTS < host rock (~1‰)	This study, Hodgskiss et al. (2018)
Mn/Sr	MTS < host rock	This study, Hodgskiss et al. (2018)
Mg/Ca	MTS < host rock	This study, Shen et al. (2016), Hodgskiss et al. (2018)
$\delta^{56}Fe$	MTS < host rock (~1–2‰)	Hodgskiss et al. (2018)
$\delta^{34}S_{CAS}$	Similar (~1‰)	This study
	MTS > host rock (~10‰)	Shen et al. (2016)
$\delta^{34}S_{Py}$	Similar (~1‰)	This study
$\delta^{26}Mg$	MTS < host rock (~1.6‰)	Shen et al. (2016)
I/(Ca + Mg)	MTS < host rock	Tang et al. (2023)
$^{87}Sr/^{86}Sr$	MTS < host rock	This study, Shields (2002)

985